



## Research Article

# Investigation of growth mechanism for highly oriented TiO<sub>2</sub> nanorods: the role of reaction time and annealing temperature



Bharat R. Bade<sup>1,4</sup> · Sachin Rondiya<sup>2</sup> · Somnath R. Bhopale<sup>1</sup> · Nelson Y. Dzade<sup>2</sup> · Mahesh M. Kamble<sup>3</sup> · Avinash Rokade<sup>4</sup> · Mamta P. Nasane<sup>1</sup> · Mahendra A. More<sup>1</sup> · Sandesh R. Jadkar<sup>1</sup> · Adinath M. Funde<sup>4</sup>

© The Author(s) 2019, corrected publication 2019 [OPEN](#)

## Abstract

Titanium dioxide (TiO<sub>2</sub>) is a versatile and inexpensive material for extended applicability in several scientific and technological fields including photo-catalysis for industrial waste treatment, energy harvesting, and hydrogen production. In this work, we report the synthesis of TiO<sub>2</sub> thin film using hydrothermal method and investigations on the influence of reaction time and annealing temperature on growth mechanism of the TiO<sub>2</sub> nanorods. The synthesized TiO<sub>2</sub> films were studied by using UV–visible spectroscopy, Raman spectroscopy, X-ray diffraction (XRD), scanning electron microscope and energy-dispersive X-ray spectroscopy (EDS). The XRD and Raman measurements revealed the formation of defect free and pure tetragonal TiO<sub>2</sub> rutile phase. The TiO<sub>2</sub> thin films show absorption band edge at around 420 nm in the UV–visible spectrum and exhibit direct band gap value of 2.9 eV. The TiO<sub>2</sub> nanorods are demonstrated to grow randomly on the FTO substrate with changing reaction times but grow uniformly in a flower-like pattern with increasing annealing temperature. Investigation of the field emission properties of TiO<sub>2</sub> thin films (tested as field-emitter array) estimates the turn-on and threshold field at 4.06 and 7.06 V/μm at 10 and 100 μA/cm<sup>2</sup>, respectively.

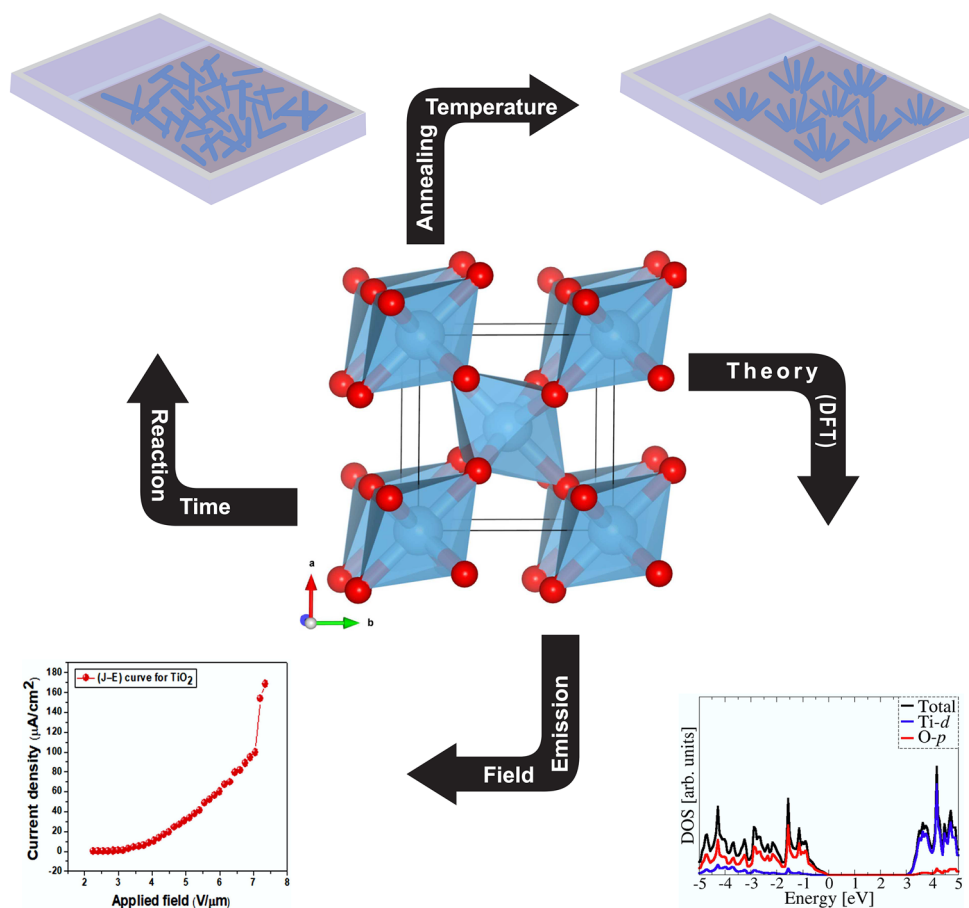
✉ Adinath M. Funde, [adinathf@gmail.com](mailto:adinathf@gmail.com) | <sup>1</sup>Department of Physics, Savitribai Phule Pune University, Pune 411007, India. <sup>2</sup>The School of Chemistry, Cardiff University, Cardiff CF10 3AT, Wales, UK. <sup>3</sup>PDEA's Anantrao Pawar College, Pirangut, Mulshi, Pune 412115, India. <sup>4</sup>The School of Energy Studies, Savitribai Phule Pune University, Pune 411007, India.



SN Applied Sciences (2019) 1:1073 | <https://doi.org/10.1007/s42452-019-0978-2>

Received: 21 June 2019 / Accepted: 23 July 2019 / Published online: 22 August 2019

## Graphic Abstract



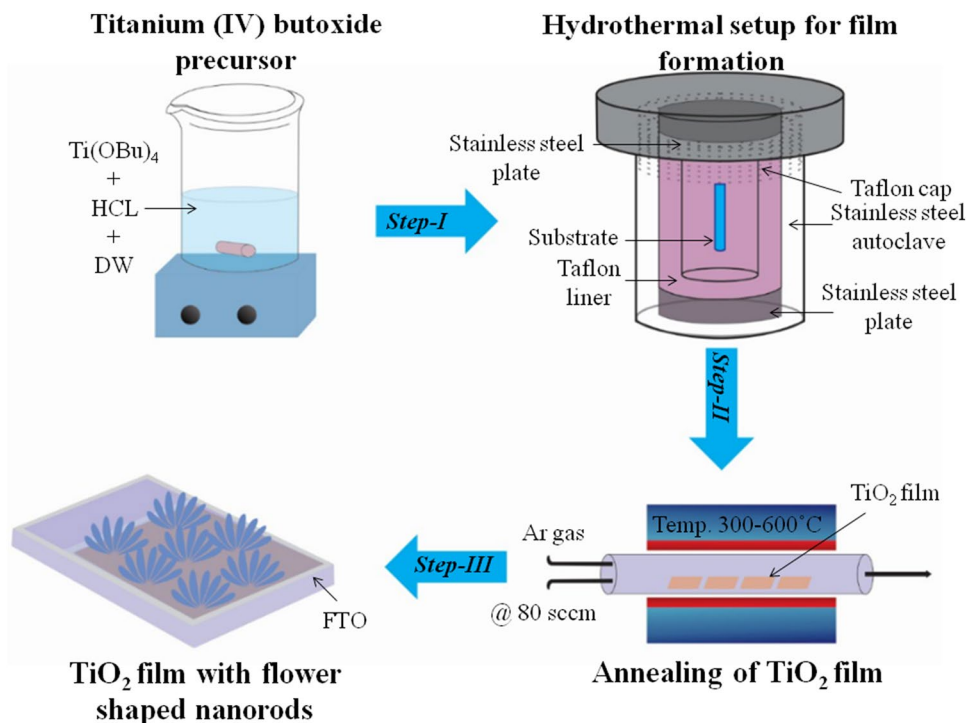
**Keywords** Titanium dioxide · Nanorods · Growth mechanism · Hydrothermal method · Density function theory · Field emission

## 1 Introduction

Nanocrystalline semiconductor materials have been attracting significant attention recently because of their unique physical and chemical properties that makes them attractive for application in industrial waste treatment (photocatalysis) and solar energy conversion (photovoltaics). Titanium dioxide (TiO<sub>2</sub>) a wide bandgap material (3.4 eV) has emerged as the most studied of these photocatalysts owing to its high degradation efficiency with almost any organic molecule and many other attractive properties, including physical and chemical stability, low cost, good thin film transparency [1–5]. These germane properties make TiO<sub>2</sub> attractive materials for several applications including solar cell (DSSCs, QDSSCs, ETA Solar Cell) [6–10], photocatalysis [11], heterogeneous catalysis, environmental hazards removal [12], ceramics and paint

industries [13–15], gas sensors [16, 17], and supercapacitors [18–20]. Besides, owing to its non-toxicity and biocompatibility, TiO<sub>2</sub> is found appropriate for application in cosmetics, food products, pharmaceuticals, and in the biomedical applications [13]. These applications of TiO<sub>2</sub> are mainly dependent on their crystalline structure, particle size, optical properties, and morphology [4, 21–23]. Thus, one of the important aspects of the development of TiO<sub>2</sub> nanoscience is our ability to control its size and morphology for specific applications such as e.g. photoconversion in solar cell and field emission arrays [24, 25]. Crystallographically, TiO<sub>2</sub> is naturally present in three phases, i.e. anatase, rutile, and brookite, with the rutile phase been the thermodynamically most stable phase. The anatase and rutile phase exhibit tetragonal crystalline structure, whereas the brookite phase has an orthorhombic structure [26, 27]. A variety of methods have been developed for the synthesis

**Fig. 1** Experimental setup of TiO<sub>2</sub> thin film formation using hydrothermal method



of TiO<sub>2</sub> nanoparticles with tailorable material properties like sol–gel [28–31], electrodeposition [32, 33], chemical vapor deposition [34], electrochemical anodic oxidation [35], spray pyrolysis [36], template-assisted [33], chemical bath deposition [37], hydrothermal methods [38, 39], and many others. Among these methods, the hydrothermal method is commonly used for synthesis of nanocrystalline TiO<sub>2</sub> as it offers the flexibility to attain different particle sizes and morphologies. Large-scale synthesis of TiO<sub>2</sub> nanoparticles with large surface area is also achievable with the hydrothermal method, hence its utilization in industrial-scale synthesis TiO<sub>2</sub> powders and thin films. Anderson et al. [40] reported the preparation of nanosize anatase and rutile TiO<sub>2</sub> by hydrothermal treatment of micro emulsions and investigated their activity for photocatalytic wet oxidation of phenol. Well-dispersed TiO<sub>2</sub> nano-crystals were synthesized by Yang et al. [41] using the hydrothermal methods. Rutile TiO<sub>2</sub> nanorods synthesized on a glass substrate at low temperature under hydrothermal condition was reported by Kakiuchi et al. [42]. Maurya et al. [43] investigated the effect of temperature on rutile TiO<sub>2</sub> using the hydrolysis method and observed that the crystallinity and density of rutile TiO<sub>2</sub> nanocrystals increases by increasing annealing temperature. The effect of repeated annealing temperature on the TiO<sub>2</sub> thin film and their structural, optical and electrical properties synthesized by dip coating sol–gel method was reported by Pakama et al. [44]. The hydrothermal synthesis of TiO<sub>2</sub> nanocrystals in

**Table 1** Process parameters employed during the deposition of TiO<sub>2</sub> thin films

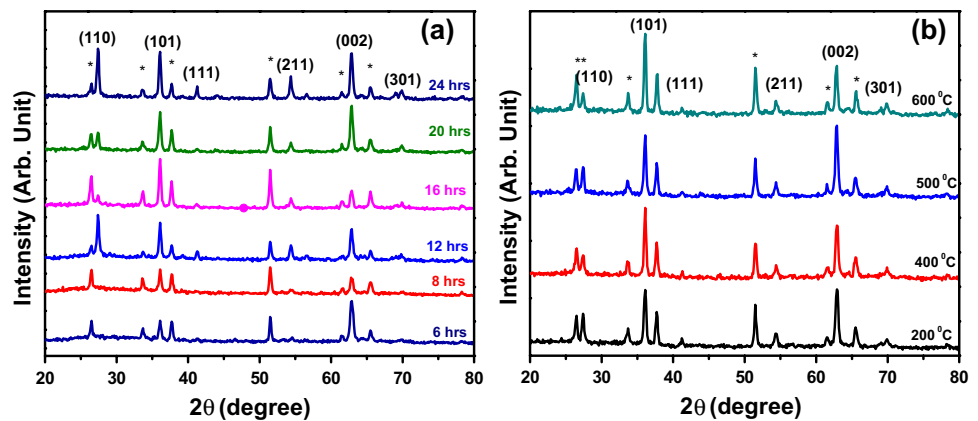
Deposition parameter	Set-I	Set-II
Concentration	50 mM Ti source	50 mM Ti source
Deposition time	<b>6–24 h</b>	20 h
Reaction temperature	150 °C	150 °C
Annealing temperature	500 °C	<b>300–600 °C</b>

The boldface text indicates the parameters varied in the set I and set II of experiments

different basic pHs and their applications in dye sensitized solar cells was reported by Anajafi et al. [45].

In the present work, synthesis of nano-structured TiO<sub>2</sub> thin films was carried out by hydrothermal technique, wherein the influence of different deposition parameters such as growth time, reaction temperature, and the film annealing temperature on the optical, structural and morphological properties have been investigated. The optical, morphological and structural characteristics of the synthesized TiO<sub>2</sub> thin films are studied by using various characterization methods such as X-ray diffraction (XRD), Raman spectroscopy, scanning electron microscopy (SEM) and UV–visible spectroscopy. The goal of the present work is to understand the correlation between the deposition parameters (reaction time and annealing temperature) and the growth mechanism of TiO<sub>2</sub> thin films. The

**Fig. 2** X-ray diffraction patterns of TiO<sub>2</sub> thin films deposited at **a** different reaction times (6 h, 8 h, 12 h, 16 h, 20 h, 24 h) and **b** different annealing temperatures. The asterisk (\*) indicate the peaks of the FTO



field-emission properties of the synthesized TiO<sub>2</sub> thin films are investigated and the results corroborated with first-principles density functional theory (DFT) calculations.

## 2 Experimental and computational details

### 2.1 Synthesis

All chemicals used in this work were analytical grade and used without further purification and treatment. For the synthesis of TiO<sub>2</sub> thin film, titanium (IV) butoxide (Sigma-Aldrich), hydrochloric acid (HCl), ethanol and distilled water were subjected to hydrothermal treatment. Commercially available FTO glass substrate was used for the growth of TiO<sub>2</sub> thin film. Titanium (IV) butoxide (5 g) was added to 10 ml HCl followed by the addition of 15 ml double distilled water. The resulting complex was then stirred at room temperature for half an hour using magnetic stirrer. The solution then transferred into locally fabricated cylindrical autoclave having dimensions 8 cm × 9 cm × 1 cm (height × diameter × thickness). The detailed structure of autoclave is schematically shown in Fig. 1. The FTO glass substrates were initially cleaned ultrasonically with double distilled water and followed by an acetone wash. Then substrates were put in ethanol solution for about 5 min. The substrates were again cleaned with double distilled water and finally given a nitrogen flush for drying. This cleaning procedure permits good adhesion of film to substrates. Then cleaned glass substrate was immersed in the solution in autoclave. After the addition of the reaction complexes and substrates, the autoclave was sealed tightly and placed in an oven at 150 °C for different reaction times ranging from 6 to 24 h for the set-I samples. The autoclave was allowed to cool naturally to room temperature. After cooling the film was taken out from autoclave and annealed at different temperature as shown in Table 1 for an hour. Two sets of films were deposited: in the first set, the TiO<sub>2</sub> thin films were

deposited at different reaction times i.e. from 6 to 24 h by keeping other parameters (concentration of the solution, deposition temperature, and annealing temperature) constant, whereas in set-II samples, the depositions was carried out with reaction time of 20 h for all the samples, with the annealing temperature varied from 300 to 600 °C and other deposition parameters were kept constant as listed in Table 1.

### 2.2 Material characterization

The average crystallite size, lattice parameter, inter planner distance, and phase identification of the deposited TiO<sub>2</sub> thin films were carried out using X-ray diffraction (XRD) pattern recorded using (Bruker D8 Advance machine, Germany) diffractometer with Cu K $\alpha$  ( $\lambda = 1.5418$  Å) radiation at a grazing angle of 1° and diffraction angle ( $2\theta$ ) ranging from 20° to 80°. Raman spectra were recorded with Raman spectroscope (Jobin–Yvon Horibra LABRAM-HR) in the range of 200–1800 cm<sup>-1</sup>. The spectrometer has backscattering geometry for detection of Raman spectrum with a resolution of 1 cm<sup>-1</sup>. The excitation source was 632.8 nm line of He–Ne laser. The possibility of laser induced crystallization in the film was avoided by keeping the power of laser beam at < 5 mW. The optical bandgap of the TiO<sub>2</sub> films was estimated from transmittance and reflectance spectra of the films deposited on commercially available FTO glass substrates and were measured using a JASCO, V-670 UV–visible spectrophotometer in the range of 200–1100 nm. The morphological characteristics of the synthesized thin films are studied by a JEOL JSM-6360-LA and Philips XL-30 scanning electron microscope.

### 2.3 Computational details

The density functional theory (DFT) calculations were performed using the Vienna Ab initio Simulation Package (VASP) [46, 47], a periodic plane wave DFT code

**Fig. 3** Raman spectra of TiO<sub>2</sub> films synthesized by hydrothermal technique process **a** at different reaction times **b** at different annealing temperature

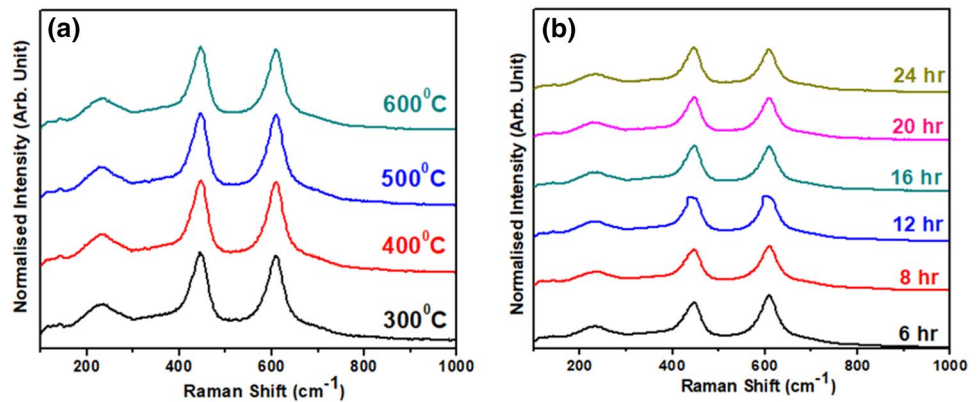
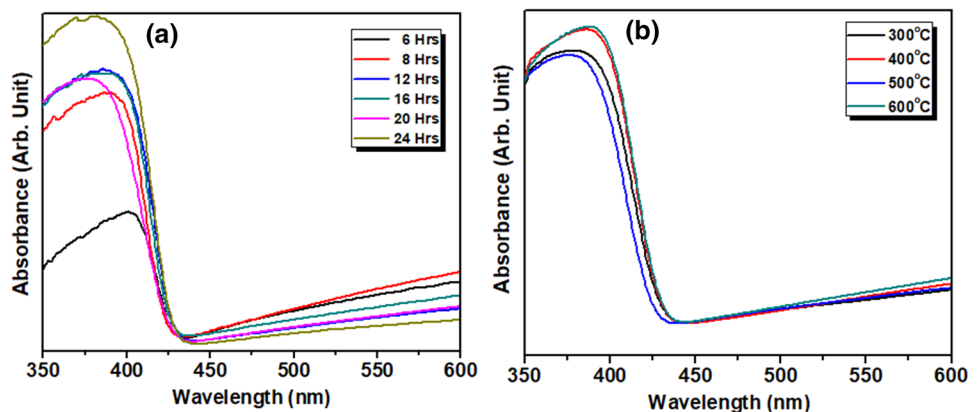


**Fig. 4** Optical absorption spectra of TiO<sub>2</sub> thin films synthesized **a** at various reaction times **b** at different annealing temperatures



which includes the interactions between the core and valence electrons using the Project Augmented Wave (PAW) method [48]. The calculations were performed using the screened hybrid functional as proposed by Heyd–Scuseria–Ernzerhof (HSE06) [49]. A percentage of the exact non-local Fock exchange ( $\alpha=0.25$ ) was added to the Perdew, Burke, and Ernzerhof (PBE) functional [50] with a screening of  $\omega=0.11$  bohr<sup>-1</sup> applied in order to partition the Coulomb potential into long range (LR) and short range (SR) terms. An energy cut-off of 600 eV, and  $9 \times 9 \times 3$  and  $9 \times 9 \times 1$  Monkhorst–Pack  $k$ -point mesh [51], was used to sample the sample the Brillouin zone of TiO<sub>2</sub> bulk and (110) surface, respectively. All calculations were deemed to be converged when the forces on all atoms were less than 0.001 eV/Å. Rutile TiO<sub>2</sub> was modelled in the simple-tetragonal structure (Fig. 4a) with space group ( $P4_2/mnm$ ) [52]. The optimized lattice constants were obtained at  $a = b = 4.598\text{Å}$ ,  $c = 2.953\text{Å}$ , in close agreement with experimental lattice constants ( $a = b = 4.594\text{Å}$  and  $c = 2.959\text{Å}$ ) [52]. The r-TiO<sub>2</sub>(110) surface was created from the optimized bulk material using the METADISE code [53], which ensures the creation of surfaces with zero dipole moment perpendicular to the surface plane [54]. In order to align the energies to the vacuum level, a slab-gap model (slab thickness of 20 Å and vacuum size of 15 Å) was

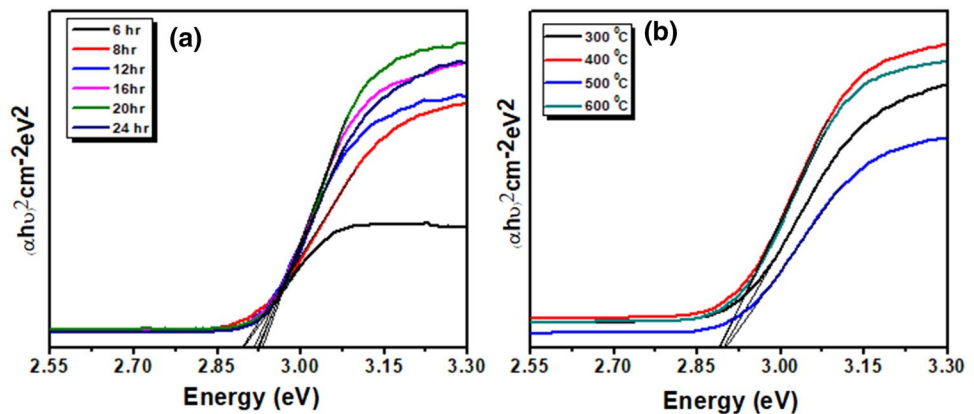
constructed and the corresponding electrostatic potential was averaged along the  $c$ -direction, using the Macro Density package [55–57], as displayed in Fig. 4(c). The work function ( $\Phi$ ), which is the minimum energy needed to remove an electron from the bulk of a material through a surface to a point outside the material was calculated as  $\Phi = V_{vacuum} - E_F$ .

### 3 Results and discussion

The XRD pattern of the set-I and set-II of TiO<sub>2</sub> thin films as described under the synthesis section are depicted in Fig. 2a, b, respectively. The peak position and relative intensity of the TiO<sub>2</sub> phases were confirmed by comparison with standard JCPDS database. The diffraction peaks located at  $2\theta = 27.4^\circ, 36.1^\circ, 41.3^\circ, 54.4^\circ, 62.9^\circ$  and  $69.9^\circ$  corresponds to the (110), (101), (111), (211), (002) and (301) [58–61] planes of rutile TiO<sub>2</sub> phases (JCPDS no. 076-1939), respectively. No peaks of other phase were detected, thus confirming the successful synthesis of high-purity rutile TiO<sub>2</sub> using hydrothermal method.

The analysis of XRD patterns confirms tetragonal rutile phase of TiO<sub>2</sub> for both the sets. The comparatively broad shoulder located at  $2\theta \sim 27.4^\circ$  is observed in all the films,

**Fig. 5** The  $(\alpha h\nu)^2$  versus  $h\nu$  plots (Tauc's plots) of  $\text{TiO}_2$  films synthesized **a** at reaction times between 6 and 24 h **b** at process temperature of  $150^\circ\text{C}$  and duration of 20 h, (with annealing at  $300^\circ\text{C}$ ,  $400^\circ\text{C}$ ,  $500^\circ\text{C}$ ,  $600^\circ\text{C}$ )



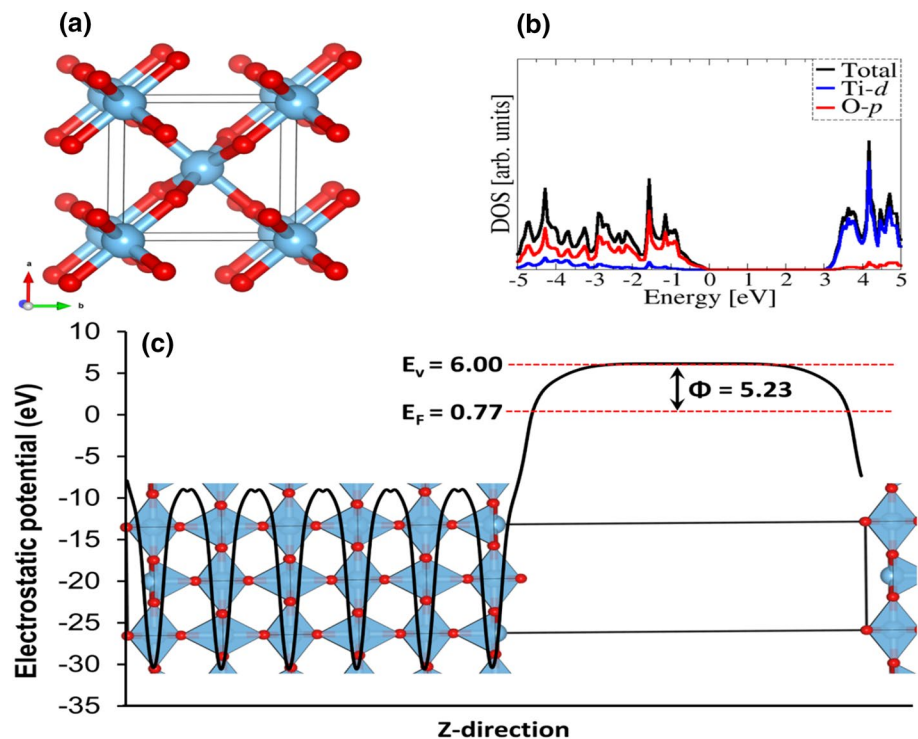
which is due to the x-ray diffraction occurring from parallel planar layers [62]. The inter planer distance for first order diffraction is  $3.26 \text{ \AA}$ , which is very well matched with the reported values ( $3.06 \text{ \AA}$ ) in literature [63]. The increased value of inter-planer distance in the present study is attributed to the presence of residual molecules intercalated between the material layers. The estimated lattice constants for the tetragonal structure is  $a = b = 4.6038 \text{ \AA}$  and  $c = 2.957 \text{ \AA}$ , which are in good agreement with the reported values in the literature [50]. The average crystallite size of  $\text{TiO}_2$  is calculated by measuring FWHM in radian corresponding to (110) peaks by using the Scherer equation  $d_{x\text{-ray}} = \frac{0.9\lambda}{\beta \cos(\theta)}$  where,  $\lambda$  is the wavelength of diffracted radiation,  $\theta$  is the Bragg angle and  $\beta$  is the line width (FWHM) in radians. The crystallite size of  $\text{TiO}_2$  was found to be in the range of 23 nm to 34 nm for the film deposited at different deposition time in set I; whereas the maximum crystallite size of 26 nm was observed at  $600^\circ\text{C}$  annealing temperature in set II. In hydrothermal processes, the deposition time and annealing temperature promote the crystallization process. The observed variation in the crystallite size may be due to the non-uniform lattice strain.

The Raman spectroscopy is a resourceful technique used for a fast and non-destructive investigation of a wide-range of Raman active modes of material. Shown in Fig. 3(a, b) are the Raman spectra for both sets of synthesized  $\text{TiO}_2$  thin films. Four prominent peaks located at  $143.2 \text{ cm}^{-1}$ ,  $235.6 \text{ cm}^{-1}$ ,  $447.1 \text{ cm}^{-1}$  and  $607.9 \text{ cm}^{-1}$  are evident and can be assigned to Raman active mode with the symmetry of  $E_g$  for rutile  $\text{TiO}_2$  characterized by the tetragonal space group of  $I4_1/amd$  and  $A_{1g}$ ,  $B_{1g}$ , and  $E_g$  which is illustrated by the tetragonal space group of  $P4_2/mnm$  for rutile  $\text{TiO}_2$  [64–69]. The two prominent maxima peaks located at  $447.1 \text{ cm}^{-1}$  ( $E_g$ ) and  $607.9 \text{ cm}^{-1}$  ( $A_{1g}$ ) correspond to O–Ti–O bending vibrations and Ti–O stretching vibrations of monoclinic rutile  $\text{TiO}_2$  phase, respectively [37, 67]. The observed prominent Raman shift at  $235.6 \text{ cm}^{-1}$ ,  $443 \text{ cm}^{-1}$ ,  $610 \text{ cm}^{-1}$ , corresponds to  $B_{1g}$ ,  $E_g$ ,  $A_{1g}$  active

mode of bulk rutile  $\text{TiO}_2$ , as reported by Begun et al. [70]. Raman shift peak positions shown in the Fig. 3 are in good agreement with those reported in the literature, indicating that synthesized  $\text{TiO}_2$  is in the rutile phase. The Raman shift peak at  $235 \text{ cm}^{-1}$  is attributed to compound vibration peak arising due to multiple phonons scattering process, which is also considered a Raman peak of rutile [71]. There is no observation of Raman active mode for brookite and other organic species impurity phases, which lead us to conclude that the hydrothermal method is the suitable for the synthesis of high-quality rutile  $\text{TiO}_2$  thin films for device fabrication.

The optical properties of  $\text{TiO}_2$  thin films grown by hydrothermal on FTO glass were investigated from UV–visible spectroscopy. Figure 4 shows the optical absorption spectra of the  $\text{TiO}_2$  thin films synthesized using hydrothermal technique at different reaction times and at different annealing temperatures. All the samples synthesized at different reaction times and at different annealing temperatures show sharp absorption edge at 423–430 nm. It also evident from Fig. 4 that the absorption edge shifts towards lower wavelength with increasing reaction times. The shift in the absorption edge towards lower wavelength is attributed to change in the  $\text{TiO}_2$  particle size. All the synthesized  $\text{TiO}_2$  thin films exhibit very strong and broad UV–visible absorption, similar to the observation by Xie et al. [38, 72] This characteristic is in agreement with the photo-protection function of the  $\text{TiO}_2$  films thus formed, making them potential candidates for solar photon capture for photo electrochemical applications. The samples however, show a low absorption above 423 nm, which can be attributed to oxygen vacancy defect formation at the surface boundaries of  $\text{TiO}_2$  [73] induced by the higher annealing temperatures. It leads to change of shape of the fundamental absorption edge of the material. As can be seen from Fig. 4, the absorption increases exponentially towards shorter wavelengths, similar to previously reported absorption spectra in the literature [74–76].

**Fig. 6** **a** Crystal structure of the rutile  $\text{TiO}_2$ ; **b** the partial density of states (PDOS) and **c** the electrostatic potential of the (110) surface along coordinate Z considering vacuum as reference energy.  $E_F$ ,  $E_v$  and  $\Phi$  correspond to the Fermi, vacuum energy and work function of the defined surface. The light blue and red balls correspond to Ti and O atoms, respectively



The optical band gap of the thin films was calculated from the dependence of the absorption coefficient ( $\alpha$ ) on the photon energy ( $h\nu$ ) using Tauc relation:  $(\alpha h\nu) = B(h\nu - E_{\text{Tauc}})^2$ , where  $B$  is Tauc's constant which is a characteristic parameter independent of photon energy,  $\alpha$  is the absorption coefficient,  $h$  is the Planck's constant,  $\nu$  is photon frequency, and  $E_{\text{Tauc}}$  is the bandgap of the material. The  $E_{\text{Tauc}}$  estimate can be deduced by plotting  $(\alpha E)^2$  versus  $E$  and extrapolating the linear portion of the plot to the energy axis. Figure 5 shows the  $(\alpha h\nu)^2$  versus  $(h\nu)$  photon energy plots for the  $\text{TiO}_2$  thin films prepared at different reaction times and annealing temperatures. The intercept of the plotted tangent gives a good approximation of the band gap energy for this material. The band gap decreases from 2.9 to 2.8 eV when deposition time increases from 6 to 24 h. It is interesting to note that these values are smaller than the reported values of synthetic  $\text{TiO}_2$  thin films [77–79]. From the absorption graph, it is confirmed that  $\text{TiO}_2$  thin film responds the UV–visible region. The optical absorption of the synthesized sample was found between 423 and 430 nm which corresponds to the band gap of  $\text{TiO}_2$  (2.9 eV).

We have employed first-principles DFT calculations to gain insight into the electronic structure and work function of rutile  $\text{TiO}_2$  as the field emission properties are strongly dependent on the work function ( $\Phi$ ) of the emitter. Shown in Fig. 6 is the crystal structure of  $\text{r-TiO}_2$  with the corresponding electronic partial density of state (PDOS). The badgap is predicted at 3.01 eV, which is good

agreement with our experimental measurements and previous DFT calculations [80–82]. An analysis of PDOS reveals that valence band edge is composed mainly of the O- $p$  whereas the and conduction band edge is composed mainly of Ti- $d$  states, indicating that  $\text{r-TiO}_2$  is a O- $p$ –Ti- $d$  charge transfer semiconductor, which agrees with earlier theoretical predictions [80–82]. The work function was obtained for the most stable (110) surface of  $\text{r-TiO}_2$ , which was cleaved from the geometrically optimized bulk. A vacuum region of length 15 Å was used in the perpendicular direction to the  $\text{r-TiO}_2$  (110) plane to avoid spurious interactions with its own periodic image. Figure 6c shows the structure of the  $\text{r-TiO}_2$ (110) surface and the corresponding electrostatic potential as a function of coordinate Z (along the  $c$ -axis). The work function ( $\Phi$ ) is calculated as the difference between the potential energy of one electron between the Fermi level ( $E_F$ ) and the vacuum level ( $E_v$ ). The vacuum level is the potential energy, approaching a nearly constant value in the energy distributions in the vacuum region, which is obtained at 6.00 eV in the present study. The work function of the  $\text{r-TiO}_2$ (110) surface is predicted at 5.23 eV, in excellent agreement with the values of 5.2–5.5 eV estimated from ultraviolet photoelectron spectroscopy measurements [83–87].

Scanning electron microscopy (SEM) is a convenient method for studying morphology and growth mechanism of the  $\text{TiO}_2$  nanorod on the FTO substrates. In the first part, we have investigated the effect of deposition time on growth mechanism of  $\text{TiO}_2$  nanorods whiles

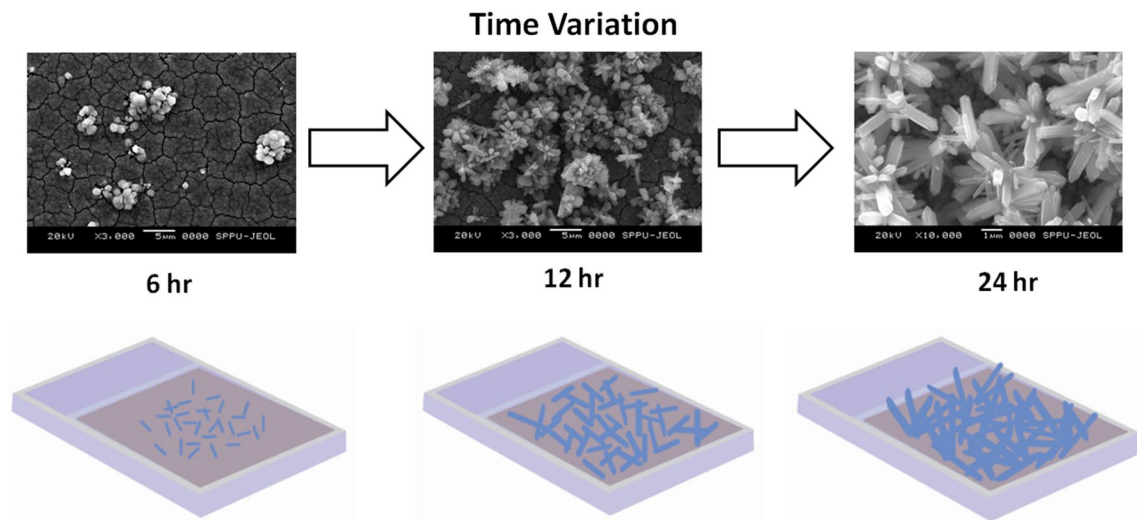


**Fig. 7** Scanning electron microscopy (SEM) micrographs of TiO<sub>2</sub> thin films at different reaction times (6, 12, and 24 h)

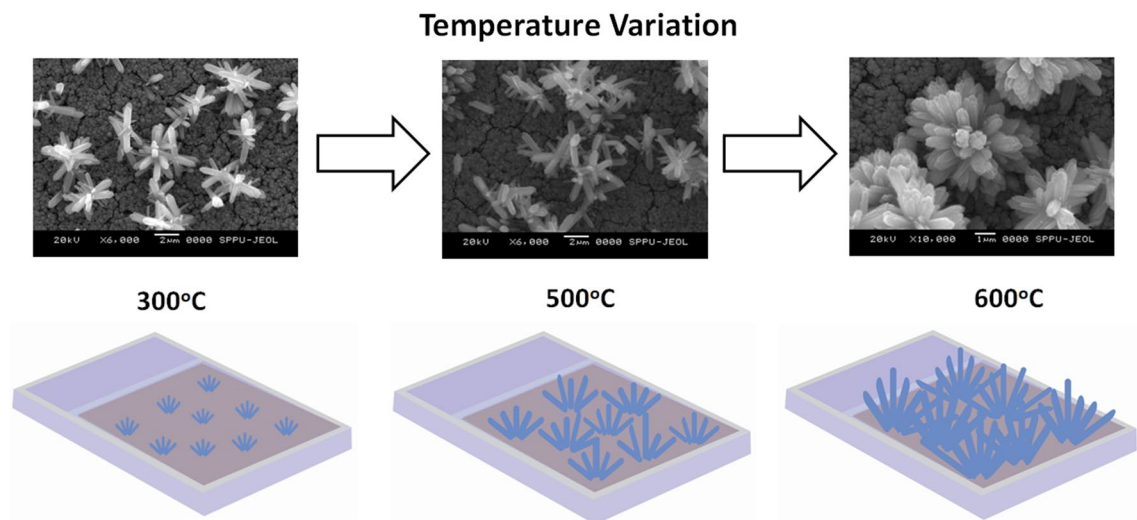


**Fig. 8** Scanning electron microscopy (SEM) micrographs of TiO<sub>2</sub> thin films at different annealing temperatures (300 °C, 500 °C, and 600 °C)

keeping other deposition parameters constant. Shown in Fig. 7 are the SEM images of TiO<sub>2</sub> films at different reaction time. It is clear from the SEM images that an increase in the reaction time leads to enhancement in the growth of TiO<sub>2</sub> nanorods. The TiO<sub>2</sub> nanorods started to grow on FTO substrate at the initial reaction time (6 h), which increased in density after 12 h and at 24 h reaction time, the growth of the TiO<sub>2</sub> nanorods covers almost the entire surface areas of the FTO substrate. Shown below each SEM image is the schematic of the nature of the growth process, revealing the growth initiation at 6 h, increased density and random growth after 12 h, and nearly full coverage of TiO<sub>2</sub> nanorods on the FTO substrate at 24 h. Although there is clear evidence of enhanced growth of TiO<sub>2</sub> nanorods

with increasing reaction times, we could not control preferential growth orientations of TiO<sub>2</sub> nanorods on FTO substrate in hydrothermal synthesis. In the second part, we have focused on the annealing temperature after synthesis of TiO<sub>2</sub> nanorods in the hydrothermal method. The Fig. 8 shows images of TiO<sub>2</sub> nanorods at different annealing temperatures. We observed clear difference in the growth process of the TiO<sub>2</sub> nanorods at annealing temperature as 300 °C, 500 °C, and 600 °C. At 300 °C, the TiO<sub>2</sub> nanorod started growing in FTO substrate in spherical microstructures. The initial stage of the growth process was limited by the premature termination of the growth surface, but with increased annealing temperature, the regularly shaped particles were transformed to onset of nano-rod



**Fig. 9** Atomic force microscopy (AFM) images of TiO<sub>2</sub> thin films at 24 h reaction time, **a** 2-dimensional (2D) AFM image and **b** 3-dimensional (3D) AFM image

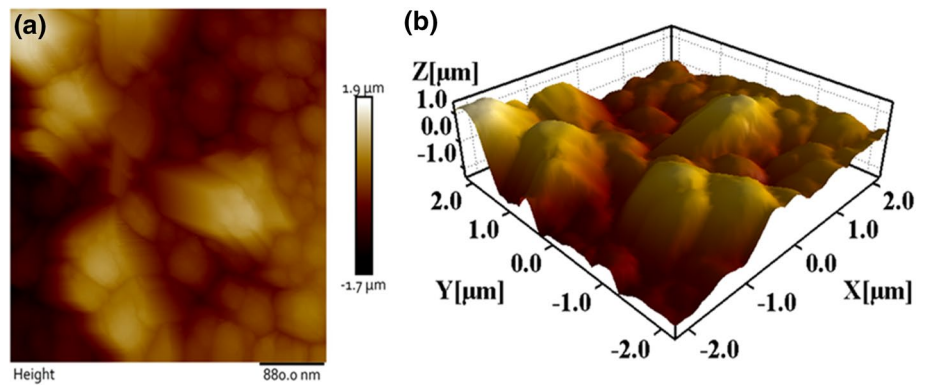
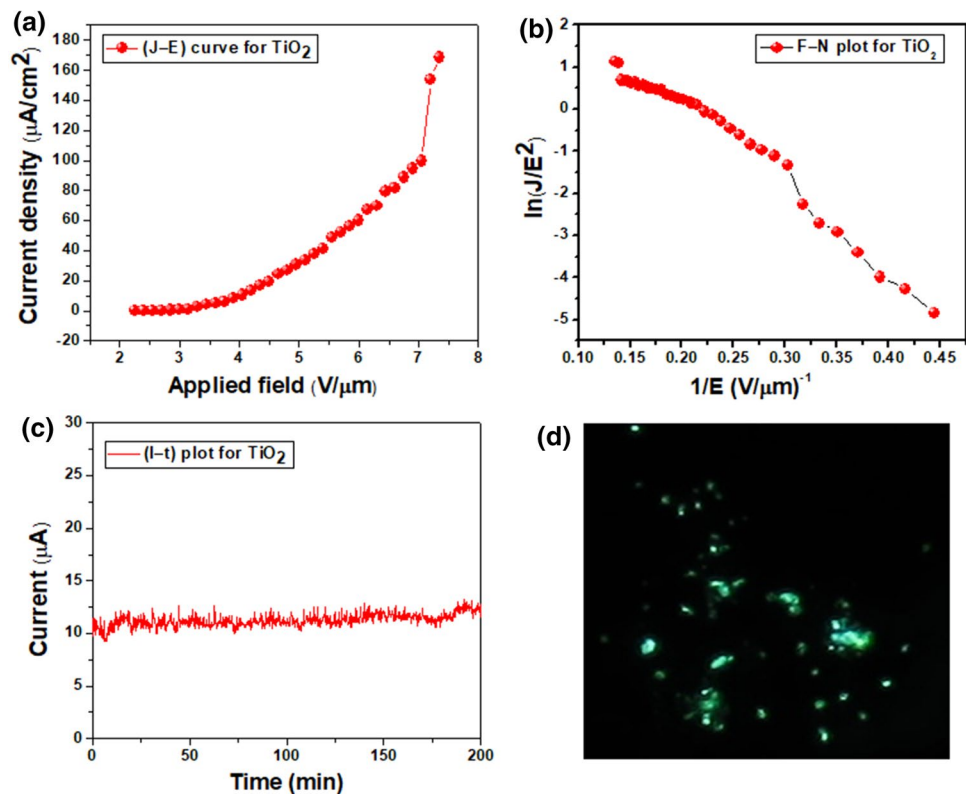


**Fig. 10** The field emission properties from TiO<sub>2</sub> nanorods **a** current density ( $J$ ) versus applied field ( $E$ ), **b** Fowler–Nordheim ( $F-N$ ) plot showing non-linear behavior, **c** current stability at 10  $\mu\text{A}$  and **d** photograph of field emission pattern



bunch morphology and further to bunch of nanorods with anchoring on the ITO substrate. Compared to the random growth nature observed with different reaction times as in set I, the growth of the TiO<sub>2</sub> nanorod is pronounced in its random nature with changing annealing temperatures as in set II. The growth of the TiO<sub>2</sub> nanorod on the FTO substrate resembles the growth of a flower in all directions. In schematic diagrams below the SEM images in Fig. 8, we demonstrate how the TiO<sub>2</sub> nanorods grow in uniform shape in a control manner. After the annealing temperature was increased to 500 °C, the TiO<sub>2</sub> nanorod density increased thereby showing the growth of nanorods from a point on the substrate and at 600 °C, the TiO<sub>2</sub> nanorods clearly look like a bunch of flowers. This demonstrates that

by varying the annealing temperature we can grow TiO<sub>2</sub> nanorod in a control manner with flower like morphology. The TiO<sub>2</sub> thin films prepared by the hydrothermal technique are without pinholes and provided continuous coverage on the substrate. The uniformly formed rod-like structures of TiO<sub>2</sub> material makes the synthesized thin films better candidates for solar cell (DSSCs) and field emitter arrays applications.

The TiO<sub>2</sub> thin films were characterized using AFM technique and shown in Fig. 9 are the 2-dimensional (2D) and 3-dimensional (3D) AFM images of the TiO<sub>2</sub> thin film at 24 h reaction time. The average roughness and root mean square (RMS) roughness for TiO<sub>2</sub> thin film estimated at 418 nm and 518 nm, respectively.

The pointed nanorod-like  $\text{TiO}_2$  structures are fascinating structures and may be suitable for several applications including as field emitter arrays. We have thus investigated the field emission properties of the  $\text{TiO}_2$  nanorods as shown in Fig. 10: (a) current density ( $J$ ) versus applied field ( $E$ ), (b) F–N plot, (c) current stability at 10  $\mu\text{A}$ , and (d) photograph of field emission pattern. The current density ( $J$ ) is defined  $J = I/A$ , where  $I$  is the emission current and  $A$  is the area of emitter. The applied field ( $E$ ) is defined as  $E = V/d$ , where  $V$  is the applied voltage, and  $d$  is the separation between the anode and cathode. According to Fowler–Nordheim (F–N) theory, in  $J$ – $E$  plot, the emission current from surface of emitter varies as exponentially [88].  $\text{TiO}_2$  nanorods  $J$ – $E$  plot showing exponential function. The electron emission quantum tunneling turn on and threshold field were found to be 4.06 and 7.06  $\text{V}/\mu\text{m}$  at emission current densities of 10 and 100  $\mu\text{A}/\text{cm}^2$  respectively of  $\text{TiO}_2$  nanorods. These values suggest that better turn on field of  $\text{TiO}_2$  nanorods are recorded as compared to the ones reported in literature [89–91]. We have obtained the maximum current density of the  $\text{TiO}_2$  nanorods to be 168  $\mu\text{A}/\text{cm}^2$  at an applied field of 7.35  $\text{V}/\mu\text{m}$ . The F–N plot of  $\text{TiO}_2$  nanorods defined by  $\ln(J/E^2)$  versus  $1/E$  (Fig. 10(b)) shows a non-linear behavior, which is consistent with the semiconductors nature of the  $\text{TiO}_2$  emitter. The emission current stability is very important for practical applications as cold cathode. The emission current ( $I$ ) versus time ( $t$ ) plot of the  $\text{TiO}_2$  nanorods at 10  $\mu\text{A}$  remained fairly stable for more than 3 h as shown Fig. 10c. The observed fluctuations and spikes in emission current may be due to the adsorption or desorption of residual gas atoms/molecules on the surface of  $\text{TiO}_2$  nanorod emitter in the presence of applied field. The field emission of  $\text{TiO}_2$  nanorods patterns is shown Fig. 10d with the tiny bright spots representing electron emission from protruding sites of  $\text{TiO}_2$  nanorods on the fluorescent screen as electron collector.

## 4 Conclusion

Large-area, very dense, and pin-hole free  $\text{TiO}_2$  nanorod thin films were successfully synthesized by a simple and cost effective hydrothermal method. The effect of reaction times and annealing temperatures on the growth mechanisms (size and shape) of the  $\text{TiO}_2$  nanorods was systematically studied. The  $\text{TiO}_2$  nanorods are demonstrated to grow randomly on the FTO substrate with changing reaction times but grow uniformly in a flower-like pattern with increasing annealing temperature. Recorded X-ray diffraction patterns, UV–VIS spectra, and Atomic force microscope images showed that the crystallinity in  $\text{TiO}_2$  thin films is significantly affected by increasing annealing temperature. The optical properties investigated

experimentally and further corroborated with first-principles density functional theory calculations show the  $\text{TiO}_2$  thin films have high absorption coefficient and a direct bandgap in the range 2.8–3.0 eV, which is slightly smaller than the bandgap of bulk rutile  $\text{TiO}_2$ . The  $\text{TiO}_2$  nanorods exhibit moderate field emission properties and have turn on field of 7.35  $\text{V}/\mu\text{m}$  and good field emission stability. These results indicate that  $\text{TiO}_2$  nanorods thin films may be promising candidates for applications in electron-emitting nano devices.

**Acknowledgements** N. Y. D. acknowledges the UK Engineering and Physical Sciences Research Council (EPSRC) for funding (Grant No. EP/S001395/1). This work has also used the computational facilities of the Advanced Research Computing at Cardiff (ARCCA) Division, Cardiff University, and HPC Wales. The author A. M. F. acknowledges Exide Industries Limited for establishment and use of facilities at EXIDE-SPPU Centre of Excellence in Energy Storage on Savitribai Phule Pune University Campus.

## Compliance with ethical standards

**Conflict of interest** On behalf of all authors, the corresponding author states that there is no conflict of interest.

**Open Access** This article is distributed under the terms of the Creative Commons Attribution 4.0 International License (<http://creativecommons.org/licenses/by/4.0/>), which permits unrestricted use, distribution, and reproduction in any medium, provided you give appropriate credit to the original author(s) and the source, provide a link to the Creative Commons license, and indicate if changes were made.

## References

- Mao SS, Chen X (2007) Selected nanotechnologies for renewable energy applications. *Int J Energy Res* 31:619–636. <https://doi.org/10.1002/er.1283>
- Mor GK, Varghese OK, Paulose M, Shankar K, Grimes CA (2006) A review on highly ordered, vertically oriented  $\text{TiO}_2$  nanotube arrays: Fabrication, material properties, and solar energy applications. *Sol Energy Mater Sol Cells* 90:2011–2075. <https://doi.org/10.1016/j.solmat.2006.04.007>
- Mills A, Hunte SL (1997) An overview of semiconductor photocatalysis. *J Photochem Photobiol A* 108:1–35. [https://doi.org/10.1016/S1010-6030\(97\)00118-4](https://doi.org/10.1016/S1010-6030(97)00118-4)
- Linsebigler AL, Lu G, Yates JT Jr (1995) Photocatalysis on  $\text{TiO}_n$  surfaces: principles, mechanisms, and selected results. *Chem Rev* 95:735–758. <https://doi.org/10.1021/cr00035a013>
- Ollis DF, Pelizzetti E, Serpone N (1991) Photocatalyzed destruction of water contaminants. *Environ Sci Technol* 25(9):1522–1529. <https://doi.org/10.1021/es00021a001>
- Herzog C, Belaidi A, Ogacho A, Dittrich T (2009) Inorganic solid state solar cell with ultra-thin nanocomposite absorber based on nanoporous  $\text{TiO}_2$  and  $\text{In}_2\text{S}_3$ . *Energy Environ Sci* 2:962–964. <https://doi.org/10.1039/B905897D>
- Ambade SB, Ambade RB, Mane RS, Lee GW, Shaikh SF, Patil SA, Joo O, Han SH, Lee SH (2013) Low temperature chemically synthesized rutile  $\text{TiO}_2$  photoanodes with high electron lifetime for organic dye-sensitized solar cells. *Chem Commun* 49:2921–2923. <https://doi.org/10.1039/c3cc00310h>

8. Yaoguang Y, Gang C, Yansong Z, Zhonghui H (2015) Recent advances in rare-earth elements modification of inorganic semiconductor based photocatalysts for efficient solar energy conversion: a review. *J Rare Earths* 33:5. [https://doi.org/10.1016/S1002-0721\(14\)60440-3](https://doi.org/10.1016/S1002-0721(14)60440-3)
9. Mali SS, Devan RS, Ma Y, Betty CA, Bhosale PN, Panmand RP, Kale BB, Jadkar SR, Patil PS, Kim JH, Hong CK (2013) Effective light harvesting in CdS nanoparticle-sensitized rutile TiO<sub>2</sub> microspheres. *Electrochim Acta* 90:666–672. <https://doi.org/10.1016/j.electacta.2012.12.017>
10. Yin X, Que W, Fei D, Xie H, He Z (2013) Effect of TiO<sub>2</sub> shell layer prepared by wet-chemical method on the photovoltaic performance of ZnO nanowires arrays-based quantum dot sensitized solar cells. *Electrochim Acta* 99:204–210. <https://doi.org/10.1016/j.electacta.2013.03.110>
11. Tang J, Durrant JR, Klug DR (2008) Mechanism of photocatalytic water splitting in TiO<sub>2</sub>. Reaction of water with photoholes, importance of charge carrier dynamics, and evidence for four-hole chemistry. *J Am Chem Soc* 130:13885–13891. <https://doi.org/10.1021/ja8034637>
12. Rasalingam S, Peng R, Koodali RT (2014) Removal of hazardous pollutants from wastewaters: applications of TiO<sub>2</sub>-SiO<sub>2</sub> mixed oxide materials. *J Nanomater* 10:42. <https://doi.org/10.1155/2014/617405>
13. Zhu RR, Wang WR, Sun XY, Liu H, Wang SL (2010) Enzyme activity inhibition and secondary structure disruption of nano-TiO<sub>2</sub> on pepsin. *Toxicol In Vitro* 24:1639–1647. <https://doi.org/10.1016/j.tiv.2010.06.002>
14. Demetrescu I, Pirvu C, Mitran V (2010) Effect of nano-topographical features of Ti/TiO<sub>2</sub> electrode surface on cell response and electrochemical stability in artificial saliva. *Bioelectrochemistry* 79:122–129. <https://doi.org/10.1016/j.bioelechem.2010.02.001>
15. Anpo M, Kamat PV (2010) Environmentally benign photocatalysts: applications of titanium oxide-based materials. Springer, New York
16. Ramadoss A, Kim SJ (2013) Vertically aligned TiO<sub>2</sub> nanorod arrays for electrochemical supercapacitor. *J Alloys Compd* 561:262–267. <https://doi.org/10.1016/j.jallcom.2013.02.015>
17. Yue L, Zhang X (2009) Structural characterization and photocatalytic behaviors of doped CeO<sub>2</sub> nanoparticles. *J Alloys Compd* 475:702–705. <https://doi.org/10.1016/j.jallcom.2008.07.096>
18. Dubal DP, Dhawale DS, More AM, Lokhande CD (2011) Synthesis and characterization of photosensitive TiO<sub>2</sub> nanorods by controlled precipitation route. *J Mater Sci* 46:2288–2293. <https://doi.org/10.1007/s10853-010-5070-7>
19. Madhugiri S, Sun B, Smirniotis PG, Ferraris JP, Balkus KJ Jr (2004) Electrospun mesoporous titanium dioxide fibers. *Microporous Mesoporous Mater* 69:77–83. <https://doi.org/10.1016/j.micromeso.2003.12.023>
20. Calleja G, Serrano DP, Sanz R, Pizarro P, Garcia A (2004) Study on the synthesis of high-surface-area mesoporous TiO<sub>2</sub> in the presence of nonionic surfactants. *Ind Eng Chem Res* 43:2485–2492. <https://doi.org/10.1021/ie030646a>
21. Pratsinis SE (1998) Flame aerosol synthesis of ceramic powders. *Prog Energy Combust Sci* 24:197–219. [https://doi.org/10.1016/S0360-1285\(97\)00028-2](https://doi.org/10.1016/S0360-1285(97)00028-2)
22. Mendoza-Anaya D, Salas P, Chavez CA, Pérez-Hernández R (2003) Microstructural characterization and morphology of TiO<sub>2</sub> for thermoluminescent applications. *Rev Mex Fis* 1(50):12–16
23. Bakardjieva S, Stengl V, Szatmary L, Subrt J, Lukac J, Murafa N, Niznansky D, Cizek K, Jirkovsky J, Petrova N (2006) Transformation of brookite-type TiO<sub>2</sub> nanocrystals to rutile: correlation between microstructure and photoactivity. *J Mater Chem* 16:1709–1716. <https://doi.org/10.1039/B514632A>
24. Jun Y, Casula MF, Sim JH, Kim SY, Cheon J, Alivisatos AP (2003) Surfactant-assisted elimination of a high energy facet as a means of controlling the shapes of TiO<sub>2</sub> nanocrystals. *J Am Chem Soc* 125:15981–15985. <https://doi.org/10.1021/ja0369515>
25. Cozzoli PD, Kornowski A, Weller H (2003) Low-temperature synthesis of soluble and processable organic-capped anatase TiO<sub>2</sub> nanorods. *J Am Chem Soc* 125:14539–14548. <https://doi.org/10.1021/ja036505h>
26. Wicaksana D, Kobayashi A, Kinbara A (1992) Process effects on structural properties of TiO<sub>2</sub> thin films by reactive sputtering. *J Vac Sci Technol A* 10:4. <https://doi.org/10.1116/1.578269>
27. Wilson GJ, Matijasevich AS, Mitchell DRG, Schulz JC, Will GD (2006) Modification of TiO<sub>2</sub> for enhanced surface properties: finite Ostwald ripening by a microwave hydrothermal process. *Langmuir* 22:2016–2027. <https://doi.org/10.1021/la052716j>
28. Zhang Q, Gao L (2003) Preparation of oxide nanocrystals with tunable morphologies by the moderate hydrothermal method: insights from rutile TiO<sub>2</sub>. *Langmuir* 19:967–971. <https://doi.org/10.1021/la020310q>
29. Tian ZR, Voigt JA, Liu J, McKenzie B, Xu H (2003) Large oriented arrays and continuous films of TiO<sub>2</sub>-based nanotubes. *J Am Chem Soc* 125:12384–12385. <https://doi.org/10.1021/ja0369461>
30. Lee S, Cho I, Lee JH, Kim DH, Kim DW, Kim JY, Shin H, Lee J, Jung OS, Park N, Kim K, Ko MJ, Hong KS (2010) Two-step sol-gel method-based TiO<sub>2</sub> nanoparticles with uniform morphology and size for efficient photo-energy conversion devices. *Chem Mater* 22:1958–1965. <https://doi.org/10.1021/cm902842k>
31. Cameron MA, Gartland IP, Smith JA, Diaz SF, George SM (2000) Atomic layer deposition of SiO<sub>2</sub> and TiO<sub>2</sub> in alumina tubular membranes: pore reduction and effect of surface species on gas transport. *Langmuir* 16:7435–7444. <https://doi.org/10.1021/la9916981>
32. Yu I, Yu X (2008) Hydrothermal synthesis and photocatalytic activity of zinc oxide hollow spheres. *Environ Sci Technol* 42:4902–4907. <https://doi.org/10.1021/es800036n>
33. Endrődi B, Kecsenovity E, Rajeshwar K, Janáky C (2018) One-step electrodeposition of nanocrystalline TiO<sub>2</sub> films with enhanced photoelectrochemical performance and charge storage. *ACS Appl. Energy Mater* 1:851–858. <https://doi.org/10.1021/acsaem.7b00289>
34. Pradhan SK, Reucroft PJ, Yang F, Dozier A (2003) Growth of TiO<sub>2</sub> nanorods by metalorganic chemical vapor deposition. *J Cryst Growth* 256:83–88. [https://doi.org/10.1016/S0022-0248\(03\)01339-3](https://doi.org/10.1016/S0022-0248(03)01339-3)
35. Yu J, Su Y, Cheng B (2007) Template-free fabrication and enhanced photocatalytic activity of hierarchical macro-/mesoporous titania. *Adv Funct Mater* 17:1984–1990. <https://doi.org/10.1002/adfm.200600933>
36. Aji BB, Shih SJ, Pradita T (2017) Controlled crystal phase of TiO<sub>2</sub> by spray pyrolysis method. *J Phys Conf Ser* 817:012021. <https://doi.org/10.1088/1742-6596/817/1/012021>
37. Mayabadi AH, Waman VS, Kamble MM, Ghosh SS, Gabhale BB, Rondiya SR, Rokade AV, Khadtare SS, Sathe VG, Pathan HM, Gosavi SW, Jadkar SR (2014) Evolution of structural and optical properties of rutile TiO<sub>2</sub> thin films synthesized at room temperature by chemical bath deposition method. *J Phys Chem Solids* 75:182–187. <https://doi.org/10.1016/j.jpcs.2013.09.008>
38. Mali SS, Betty CA, Bhosale PN, Patil PS (2011) Hydrothermal synthesis of rutile TiO<sub>2</sub> with hierarchical microspheres and their characterization. *CrystEngComm* 13:6349–6351. <https://doi.org/10.1039/C1CE05928A>
39. Shinde DB, Jagadale SK, Mane RK, Mane RM, Ghanwat VB, Khot KV, Mali SS, Hong CK, Bhosale PN (2015) Time dependent facile hydrothermal synthesis of TiO<sub>2</sub> nanorods and their photoelectrochemical applications. *J Nanomed Nanotechnol* 57:2157–7439. <https://doi.org/10.4172/2157-7439.S7-004>
40. Andersson M, Oesterlund L, Ljungstrom S, Palmqvist A (2002) Preparation of nanosize anatase and rutile TiO<sub>2</sub> by hydrothermal

- treatment of microemulsions and their activity for photocatalytic wet oxidation of phenol. *J Phys Chem B* 106(41):10674–10679. <https://doi.org/10.1021/jp025715y>
41. Yang J, Mei S, Ferreira JMF (2002) Hydrothermal synthesis of well-dispersed TiO<sub>2</sub> nano-crystals. *J Mater Res* 17:2197–2200. <https://doi.org/10.1557/JMR.2002.0323>
  42. Kakiuchi K, Hosono E, Imai H, Kimura T, Fujihara S (2006) {1 1 1}-faceting of low-temperature processed rutile TiO<sub>2</sub> rods. *J Cryst Growth* 293:541–545. <https://doi.org/10.1016/j.jcrysgro.2006.06.004>
  43. Maurya A, Chauhan P, Mishra SK, Srivastav RK (2011) Structural, optical and charge transport study of rutile TiO<sub>2</sub> nanocrystals at two calcination temperatures. *J. Alloys Compd* 509:8433–8440. <https://doi.org/10.1016/j.jallcom.2011.05.108>
  44. Pakma O, Serin N, Serin T (2009) The effect of repeated annealing temperature on the structural, optical, and electrical properties of TiO<sub>2</sub> thin films prepared by dip-coating sol-gel method. *J Mater Sci* 44:401–407. <https://doi.org/10.1007/s10853-008-3145-5>
  45. Anajafi Z, Marandi M, Taghavinia N (2015) Hydrothermal synthesis of TiO<sub>2</sub> nanocrystals in different basic pHs and their applications in dye sensitized solar cells. *Physica E* 70:113–120. <https://doi.org/10.1016/j.physe.2015.02.023>
  46. Kresse G, Joubert D (1999) From ultrasoft pseudopotentials to the projector augmented-wave method. *Phys Rev B* 59(3):1758–1775. <https://doi.org/10.1103/PhysRevB.59.1758>
  47. Kresse G, Furthmüller J (1996) Efficient iterative schemes for ab initio total-energy calculations using a plane-wave basis set. *Comput Mater Sci* 6:15. <https://doi.org/10.1103/PhysRevB.54.11169>
  48. Blöchl PE (1994) Projector augmented-wave method. *Phys Rev B* 50:17953. <https://doi.org/10.1103/PhysRevB.50.17953>
  49. Krukau AV, Vydrov OA, Izmaylov AF, Scuseria GE (2006) Influence of the exchange screening parameter on the performance of screened hybrid functional. *J Chem Phys* 125:224106. <https://doi.org/10.1063/1.2404663>
  50. Perdew JP, Burke K, Ernzerhof M (1997) Generalized gradient approximation made simple. *Phys Rev Lett* 78:1396. <https://doi.org/10.1103/PhysRevLett.77.3865>
  51. Monkhorst HJ, Pack JD (1976) Special points for Brillouin-zone integrations. *Phys Rev B* 13:5188. <https://doi.org/10.1103/PhysRevB.13.5188>
  52. Abrahams SC, Bernstein JL (1971) Rutile: normal probability plot analysis and accurate measurement of crystal structure. *J Chem Phys* 55:3206. <https://doi.org/10.1063/1.1676569>
  53. Watson GW, Kelsey ET, de Leeuw NH, Harris DJ, Parker SC (1996) Atomistic simulation of dislocations, surfaces and interfaces in MgO. *Chem Soc Faraday Trans* 92:433–438. <https://doi.org/10.1039/ft9969200433>
  54. Tasker PW (1979) The stability of ionic crystal surfaces. *J Phys C Solid State Phys* 12:4977. <https://doi.org/10.1088/0022-3719/12/22/036>
  55. Walsh A, Butler KT (2013) Prediction of electron energies in metal oxides. *Acc Chem Res* 47:364–372. <https://doi.org/10.1021/ar400115x>
  56. Ganose AM, Butler KT, Walsh A, Scanlon DO (2016) Relativistic electronic structure and band alignment of BiSb and BiSe: candidate photovoltaic materials. *J Mater Chem A* 4:2060. <https://doi.org/10.1039/C5TA09612J>
  57. Wu L, Dzade NY, Gao L, Scanlon DO, Öztürk Z, Hollingsworth N, Weckhuysen BM, Hensen EJM, de Leeuw NH, Hofmann JP (2017) Enhanced photoresponse of FeS<sub>2</sub> films: the role of marcasite-pyrite phase junctions. *J Adv Mater* 28:9602–9607. <https://doi.org/10.1002/adma.201602222>
  58. Sharma A, Karn RK, Pandiyan SK (2014) Synthesis of TiO<sub>2</sub> nanoparticles by sol-gel method and their characterization. *J Basic Appl Eng Res* 1:1–5
  59. Xia X, Peng S, Bao Y, Wang Y, Lei B, Wang Z, Huang Z, Gao Y (2018) Control of interface between anatase TiO<sub>2</sub> nanoparticles and rutile TiO<sub>2</sub> nanorods for efficient photocatalytic H<sub>2</sub> generation. *J Power Sources* 376:11–17. <https://doi.org/10.1016/j.jpowsour.2017.11.067>
  60. Thamaphat K, Limsuwan P, Ngotawornchai B (2008) Phase characterization of TiO<sub>2</sub> powder by XRD and TEM. *Kasetsart J (Nat Sci)* 42:357–361
  61. Wang Y, Li L, Huang X, Li Q, Li G (2015) Electronic supplementary information (ESI) available for: new understanding of fluorinated TiO<sub>2</sub> (brookite, anatase and rutile) nanoparticles as efficient photocatalytic redox catalysts. *RSC Adv* 5:34302. <https://doi.org/10.1039/c4ra17076h>
  62. Vorontsov AV, Tsybulya SV (2018) Influence of nanoparticles size on XRD patterns for small monodisperse nanoparticles of Cu<sup>0</sup> and TiO<sub>2</sub> anatase. *Ind Eng Chem Res* 57:2526–2536. <https://doi.org/10.1021/acs.iecr.7b04480>
  63. Miao L, Jin P, Kaneko K, Terai A, Nabatova-Gabain N, Tanemur S (2003) Preparation and characterization of polycrystalline anatase and rutile TiO<sub>2</sub> thin films by rf magnetron sputtering. *Appl Surf Sci* 212–213:255–263. [https://doi.org/10.1016/S0169-4332\(03\)00106-5](https://doi.org/10.1016/S0169-4332(03)00106-5)
  64. Mazza T, Barborini E, Piseri P, Milani P (2007) Raman spectroscopy characterization of TiO<sub>2</sub> rutile nanocrystals. *Phys Rev B* 75:045416. <https://doi.org/10.1103/PhysRevB.75.045416>
  65. Ocana M, Garcia-Ramos JV, Serna CJ (1992) Low-temperature nucleation of rutile observed by raman spectroscopy during crystallization of TiO<sub>2</sub>. *J Am Ceram Soc* 75(171):2010–2012. <https://doi.org/10.1111/j.1151-2916.1992.tb07237.x>
  66. Ohsaka T, Izumi F, Fujiki Y (1978) raman spectrum of anatase, TiO<sub>2</sub>. *J Raman Spectrosc* 7:321–324. <https://doi.org/10.1002/jrs.1250070606>
  67. Ma HL, Yang JY, Dai Y, Zhang YB, Lu B, Ma GH (2007) Raman study of phase transformation of TiO<sub>2</sub> rutile single crystal irradiated by infrared femtosecond laser. *Appl Surf Sci* 253:7497–7500. <https://doi.org/10.1016/j.apsusc.2007.03.047>
  68. Tamilselvan V, Yuvaraj D, Kumar RR, Rao KN (2012) Growth of rutile TiO<sub>2</sub> nanorods on TiO<sub>2</sub> seed layer deposited by electron beam evaporation. *Appl Surf Sci* 258:4283–4287. <https://doi.org/10.1016/j.apsusc.2011.12.079>
  69. Meng X, Shin D, Yu SM, Jung JH, Kim HI, Lee HM, Han Y, Bho-raskar V, Yoo J (2011) Growth of hierarchical TiO<sub>2</sub> nanostructures on anatase nanofibers and their application in photocatalytic activity. *CrystEngComm* 13:3021. <https://doi.org/10.1039/C0CE00765J>
  70. Begun GM, Bamberger CE (1989) Raman spectroscopic observation of laser-induced oxidation of transition-metal borides, carbides, and nitrides. *Appl Spectrosc* 43:134–138. <https://doi.org/10.1366/0003702894201914>
  71. Yan J, Wu G, Guan N, Li L, Li Z (2013) Understanding the effect of surface/bulk defects on the photocatalytic activity of TiO<sub>2</sub>: anatase versus rutile. *Phys Chem Chem Phys* 15:10978–10988. <https://doi.org/10.1039/c3cp50927c>
  72. Xie C, Yang S, Shi J, Niu C (2016) Highly Crystallized C-doped mesoporous anatase TiO<sub>2</sub> with visible light photocatalytic activity. *Catalysts* 6:117. <https://doi.org/10.3390/catal6080117>
  73. Thompson TL, Yates JT Jr (2006) Surface science studies of the photoactivation of TiO<sub>2</sub>s new photochemical processes. *Chem Rev* 106:4428–4453. <https://doi.org/10.1021/cr050172k>
  74. Shirke BS, Korake PV, Hankare PP, Bamane SR, Garadkar KM (2011) Synthesis and characterization of pure anatase TiO<sub>2</sub> nanoparticles. *J Mater Sci Mater Electron* 22:821–824. <https://doi.org/10.1007/s10854-010-0218-4>

75. Wang C, Geng A, Guo Y, Jiang S, Qu X, Li L (2006) A novel preparation of three-dimensionally ordered macroporous M/Ti = Zr or Ta) mixed oxide nanoparticles with enhanced photocatalytic activity. *J Colloid Interface Sci* 301:236–247. <https://doi.org/10.1016/j.jcis.2006.05.002>
76. Vijayalakshmi R, Rajendran V (2012) Synthesis and characterization of nano-TiO<sub>2</sub> via different methods. *Arch Appl Sci Res* 4(2):1183–1190
77. Tripathi AK, Singh MK, Mathpal MC, Mishra SK, Agarwal A (2013) Study of structural transformation in TiO<sub>2</sub> nanoparticles and its optical properties. *J Alloys Compd* 549:114–120. <https://doi.org/10.1016/j.jallcom.2012.09.012>
78. Tripathi AK, Mathpal MC, Kumar P, Singh MK, Mishra SK, Srivastava RK, Chung JS, Verma G, Ahmad MM, Agarwal A (2014) Synthesis based structural and optical behavior of anatase TiO<sub>2</sub> nanoparticles. *Mater Sci Semicond Process* 23:136–143. <https://doi.org/10.1016/j.mssp.2014.02.041>
79. Kawahara T, Ozawa T, Iwasaki M, Tada H, Ito S (2003) Photo-catalytic activity of rutile–anatase coupled TiO<sub>2</sub> particles prepared. *J Colloid Interface Sci* 267:377–381. [https://doi.org/10.1016/S0021-9797\(03\)00755-0](https://doi.org/10.1016/S0021-9797(03)00755-0)
80. Scanlon DO, Dunnill CW, Buckeridge J, Shevlin SA, Logsdail AJ, Woodley SM, Catlow CRA, Powell MJ, Palgrave RG, Parkin IP, Watson GW, Keal TW, Sherwood P, Walsh A, Sokol AA (2013) Band alignment of rutile and anatase TiO<sub>2</sub>. *Nat Mater* 12:798–801. <https://doi.org/10.1038/nmat3697>
81. Pfeifer V, Erhart P, Li S, Rachut K, Morasch J, Brötz J, Reckers P, Mayer T, Rühle S, Zaban A, Seró IM, Bisquert J, Jaegermann W, Klein A (2013) Energy band alignment between anatase and rutile TiO<sub>2</sub>. *J Phys Chem Lett* 4(23):4182–4187. <https://doi.org/10.1021/jz402165b>
82. Pascual J, Camassel J, Mathieu H (1978) Fine structure in the intrinsic absorption edge of TiO<sub>2</sub>. *Phys Rev B* 18:5606–5614. <https://doi.org/10.1103/PhysRevB.18.5606>
83. Borodin A, Reichling M (2011) Characterizing TiO<sub>2</sub>(110) surface states by their work function. *Phys Chem Chem Phys* 13:15442–15447. <https://doi.org/10.1039/c0cp02835e>
84. Chung YW, Lo WJ, Somorjai GA (1977) Low energy electron diffraction and electron spectroscopy studies of the clean (110) and (100) titanium dioxide (rutile) crystal surfaces. *Surf Sci* 64:588. [https://doi.org/10.1016/0039-6028\(77\)90064-4](https://doi.org/10.1016/0039-6028(77)90064-4)
85. Onishi H, Aruga T, Egawa C, Iwasawa Y (1988) Adsorption of CH<sub>3</sub>OH, HCOOH and SO<sub>2</sub> on TiO<sub>2</sub> (110) and stepped TiO<sub>2</sub> (441) surfaces. *Surf Sci* 193(1–2):33–46. [https://doi.org/10.1016/0039-6028\(88\)90321-4](https://doi.org/10.1016/0039-6028(88)90321-4)
86. Onda K, Li B, Petek H (2004) Two-photon photoemission spectroscopy of TiO<sub>2</sub>(110) surfaces modified by defects and O<sub>2</sub> or H<sub>2</sub>O adsorbates. *Phys Rev B* 70:045415. <https://doi.org/10.1103/PhysRevB.70.045415>
87. Schierbaum K, Fischer S, Wincott P, Hardman P, Dhanak V, Jones G, Thornton G (1997) Electronic structure of Pt overlayers on (1 × 3) reconstructed TiO<sub>2</sub>(100) surfaces. *Surf Sci* 391:196–203. [https://doi.org/10.1016/S0039-6028\(97\)00483-4](https://doi.org/10.1016/S0039-6028(97)00483-4)
88. Zubair M, Ang YS, Ang LK (2018) Fractional Fowler–Nordheim law for field emission from rough surface with nonparabolic energy dispersion. *IEEE Trans Electron Devices* 65:2089–2095. <https://doi.org/10.1109/TED.2017.2786020>
89. Chavan PG, Shende SV, Joag DS, More MA (2011) Photo-enhanced field emission study of TiO<sub>2</sub> nanotubes array. *Ultramicroscopy* 111:415–420. <https://doi.org/10.1016/j.ultra.2010.11.001>
90. Xiang B, Zhang Y, Wang Z, Luo XH, Zhu YW, Zhang HZ, Yu DP (2005) Field-emission properties of TiO<sub>2</sub> nanowire arrays. *J Phys D Appl Phys* 38:1152–1155. <https://doi.org/10.1088/0022-3727/38/8/009>
91. Didwal PN, Chikate PR, Bankar PK, More MA, Devan RS (2019) Intense field electron emission source designed from large area array of dense rutile TiO<sub>2</sub> nanopillars. *J Mater Sci Mater Electron* 30:2935–2941. <https://doi.org/10.1007/s10854-018-00570-9>

**Publisher's Note** Springer Nature remains neutral with regard to jurisdictional claims in published maps and institutional affiliations.